Oxygen nonstoichiometry and electrical transport properties of $Pr_{1-x}Ca_xMnO_3$ ceramics

C. Pithan [a, b, *], Y. Iida [c], J. Dornseiffer [d], A. Tsubouchi [c] and R. Waser [a, e]

[a] *Peter Grünberg Institute, PGI-7 – Electronic Materials, Forschungszentrum Jülich GmbH & Jülich Aachen Research Alliance of Fundamentals on Future Information Technology (JARA-FIT), Jülich, Germany*
[b] *Department of Materials Engineering, National Pingtung University of Science and Technology, Pingtung, Taiwan, R.O.C.*
[c] *Murata Manufacturing Co., Ltd., Kyoto, Japan*
[d] *Institute of Energy and Climate Research, IEK-1 – Materials Synthesis and Processing, Forschungszentrum Jülich GmbH*
[e] *Institut für Werkstoffe der Elektrotechnik II, RWTH Aachen, Aachen, Germany*
[*] Corresponding author

KEYWORDS

PCMO: $(Pr_{1-x}Ca_x)MnO_3$
Crystal chemistry
Oxygen-deficiency
Iodometry
Thermogravimetric analysis
DC-conductivity
Seebeck-effect

ABSTRACT

The defect chemistry of solid solutions formed by the two orthorhombic perovskite-type compounds $CaMnO_3$ and $PrMnO_3$ is strongly determined by mixed valence states emerging from the presence of trivalent or tetravalent Mn-cations, Mn^{3+} and Mn^{4+}. Both, thermogravimetric analysis as well as measurements of DC-conductivity at elevated temperatures in dependence of the partial pressure of oxygen quantitatively reveal the extent of oxygen vacancy formation in highly densified ceramic pellets originally consolidated by sintering in pure oxygen O_2. Iodometry additionally serves to analyse the average valence state of Mn-cations and thus of the deficiency in oxygen after targeted thermal treatments under specific redox conditions. The determination of electrical transport properties including also the careful inspection of the Seebeck-effect for such specimens demonstrates that the mobility of electrons is drastically reduced when the number of oxygen vacancies increases. For the specific composition $Pr_{0.7}Ca_{0.3}MnO_3$, an oxide potentially relevant for resistively switching memory device applications, this is the case when the deficiency in oxygen exceeds a concentration of 1000 ppm. Detailed crystallographic studies based on refined neutron-diffraction experiments for reduced ceramic material suggest, that the reduction in electron transfer rates between tri- and tetravalent cations of manganese originates from an anisotropy effect: In the case of comparatively large oxygen deficiency, vacancies preferentially form on lattice sites in the equatorial plane of MnO_6-octahedra rather than on their apices.

1. Introduction

Many manganite-based compounds formed by rare- in combination with alkaline-earth metals – such as for instance praseodymium and calcium – crystalize in one of the perovskite-type family of lattice symmetries and reveal a versatility remarkably rich regarding crystal chemistry and physics [1-5]. They offer an extensive but also quite complex variety of possible structural and crystallographic arrangements partially originating from the possible realization of charge-, spin- or orbital-ordered states, the eventual occurrence of Jahn-Teller coupling and, of course, from mixed valence states of the cations of the transition metal manganese Mn. In consequence, this group of oxides manifests a considerable number of highly interesting and in part also technologically relevant electrical, magnetic or optical properties [1-6] that have been attracting extensive scientific attention for more than half a century since their initial reference by some early reports from Philips Research Laboratories [7-10].

A likewise widespread field of potential materials applications has also been reported and discussed in the past, including solid electrolyte cathodes, e.g. based on $La_{1-x}Sr_xMnO_3$ for fuel cells [11], just to mention one prominent illustrative example of current relevance here. But, more generally, some compounds also seem to be attractive for the use as heterogeneous gas catalysts [12-15].

Moreover, perovskite-type manganite compounds with mixed valence states may exhibit an extraordinarily pronounced magnetoresistive effect [16-21]: Upon the application of an external magnetic field they drastically change their electrical conductivity and have therefore been projected for the use in magnetic sensors or in data storage devices [22] too.

Another, related and recently emerging area of research representing growing scientific interest constitute materials that might find applications in a future generation of fast, miniaturized, non-volatile and energy-efficient memory devices with large storage capacity, where resistivity is rather controlled through an external electric and not through a magnetic stimulus (ReRAM: Resistive Random-Access Memory) [23]. Phenomenologically, such promising resistively switching materials show a reversible and reproducible, hysteretic change of conductivity between two (bistable) – or sometimes even more – distinct states in response to an external electric inducement, often driven through a pulsed electric field, in practice. It is essential to emphasize, that the corresponding resistance states are non-volatile and remain preserved even if the external field is removed: Their retention still persists without external power connection.

The physical effect of resistive switching has been known for a long time [24] and observed since then to occur in many different insulating, non-metallic, mainly inorganic compounds such as initially for Al_2O_3 [24], several years later for NiO [25, 26], Nb_2O_5 [27, 28], TiO_2 [29] and for numerous further materials, including other oxides, chalcogenides, nitrides or fluorides [30]. Equally, oxides of higher order than binary ones such as perovskite-type compounds represent well established examples of resistively switching materials for quite a long period of time [31-41].

It is remarkable, that the phenomenon of resistive switching is apparently not directly related to any specific crystallographic order, symmetry or stoichiometric ratio of a particular lattice structure: it exists for sub-oxides, e.g. Nb_xO_y [42] or for amorphous materials [43, 44] as well.

The original discovery of the effect in single crystals of $Pr_{0.7}Ca_{0.3}MnO_3$ (PCMO), a material that was formerly mainly known to have exceptional magnetoresistive properties, was reported in 1997 by Asamitsu et al. [31]. Quite similar, chemically related compounds have also been found to exhibit electric field driven resistive switching: $Sm_{0.5}Sr_{0.5}MnO_3$ [32], $Nd_{0.5}Sr_{0.5}MnO_3$, $Nd_{0.5}Ca_{0.5}MnO_3$ or $Y_{0.5}Ca_{0.5}MnO_3$ [33], as well as $La_{0.7}Ca_{0.3}MnO_3$ [38-40]. Solid solutions of Pr-Ca–manganites with various compositions, however, constitute the ceramic system that is explored in the present study.

In the traditional experimental realization resistive switching phenomena appearing in an originally insulating material become evident from the current-voltage characteristics recorded for a simple, vertical and planar two terminal capacitor-like MIM (metal-insulator-metal) stacked configuration: In an electric field of increasing strength a sudden, anomalous drop of insulation resistivity ("negative resistivity") is generally observed at a particular threshold limit of the external stimulus. A corresponding drastic increase of the leakage current consequently occurs, when this more conductive state is established. In contrast, however, to a dielectric breakdown that is usually provoked at much larger external electric stresses and where the insulation resistance is permanently and incurably damaged, the collapse to the low resistance state (LRS) can be switched back to a distinct, more insulating high resistivity state (HRS). Depending on whether the switching characteristics depend on both, direction and amplitude of the field, or just on the amplitude only, bipolar or unipolar behaviour are distinguished. The switching event itself can take place locally along filamentary pathways or more uniformly in a spatially "delocalized" planar manner distributed over the entire lateral interface between the electrode and the insulating material [45].

The exact microscopic mechanism generating this rather complicated behaviour is not fully understood in all details: Particulars are still under controversial scientific debate, but it is well accepted [46-48], essentially, that redox-type processes [48] in a transition layer just beneath the anode play a central role.

Soon after the initial report published on PCMO-single crystals by Asamitsu et al. [31], Liu et al. [49] initially examined bipolar resistive switching PCMO thin films grown by physical laser deposition (PLD) epitaxy and tried to answer questions regarding the origin of the large resistivity ratio between the HRS and LRS, exceeding a factor of 17, they observed. Their speculative interpretation explaining the LRS as a volume-effect of PCMO grounds on the assumption of highly conductive percolating ferromagnetic clusters of low electric resistivity. According to their view conductive filaments are formed within an insulating paramagnetic matrix upon directional reorganization of individual clusters under the action of an electric field. Baikalov et al. [50] investigated sputtered PCMO thin films prepared at relatively high partial pressures of oxygen in argon and used Ag-electrodes as contacts. Their study demonstrates that the large increase in resistance upon switching – appearing to be inconsistent with "bulk-values" [51, 52] – must preferentially occur as an interface effect close to the metallic contact and suggests field induced electrochemical migration as a driving mechanism. Later reports confirm the dominating role of uniform insulating active layers of only several nm thickness that form a non-ohmic contact resistance at the oxide-electrode interface: In consequence, electrical biasing does not only modulate resistance but also capacitance [53]. Voltage dependent measurements of capacitance [54, 55] support the existence of such transition layers and give an estimate about their thickness. Large capacitance values indicate a layer narrow enough for charge carriers to tunnel from the oxide into the metallic electrode (LRS). On the other hand, a wider layer resulting in a small capacitive contribution may act as a barrier for electric transport (HRS). Chen et al. [55] visualized the spatial distribution of resistance changes in PCMO thin films by scanning Kelvin probe microscopy: jumps of the electric potential evidence major variations localized at the interface of PCMO to the electrode associated with the pile up of mobile charge species. The switching effect seems to rely on a tuneable tunnelling barrier assumed to be modulated in thickness [56] – between a thicker HRS and a thinner LRS – by shuffling oxygen vacancies forth and backwards. That indeed motion and pileup of oxygen anions via vacancies represent major active processes was shown by Nian and colleagues [57] who compared resistance relaxation in thin films sputtered in either oxygen-rich or oxygen-deficient ambient. In their study the authors found, that relaxation times and activation energies of resistance change quantitatively correspond to oxygen transport by diffusion under electric pulsing.

In this context the electrode metal deposited, its choice, work-function [58] and affinity to oxidation [59] crucially influence the hysteretic behaviour of resistive switching [58-61]. Less noble metals than Pt or Au such as Ag, Ti or Ta act as getter and extract oxygen out of PCMO generating an oxygen deficient zone beneath a thin passivation layer formed [62, 63]. In summary, PCMO located just below this actively switching anodized layer seems to serve as a reservoir for oxygen anions that diffuse towards the metallic electrode upon the application of an electric bias.

Because oxygen vacancies take a central part in the elementary switching mechanisms of PCMO obviously, the conditions of their formation, their concentration and mobility, as well as their relation to conductivity are essential to know. Beyond this fundamental aspect, a profound understanding for the driving mechanisms of resistive switching in PCMO is desirable. Questions about how ionic rearrangement or migration of oxygen exactly modulate the resistance of a local, interfacial region in a resistively switching medium and converts an original insulator to a conductor have to answered in order to further optimize ReRAM devices based on this material from a more practical perspective too. In particular, issues related to device reliability, reproducibility and stable retention behaviour upon electric cycling are believed to be closely dependent on the crystal chemistry of PCMO [47].

Some previous studies describe defect chemical aspects of chemically or structurally related compounds like $CaMnO_3$ [64], $LaMnO_3$ [65-77] or $La_xCa_{1-x}MnO_3$ [70], $La_xSr_{1-x}MnO_3$ [66-71, 73-77], and $La_xBa_{1-x}MnO_3$ [70], focussing mainly on oxygen nonstoichiometry.

They primarily report the thermodynamic treatment of metal vacancy formation, electric conduction and thermo-electric power in the case of oxygen-deficiency or -excess.

However, no detailed and systematic study for the system $Pr_xCa_{1-x}MnO_3$ has been presented so far describing quantitatively under which thermodynamic circumstances vacancies of oxygen form and how the crystal chemistry is related to electric conduction through small polaron hoping in these materials. The current study addresses the methodical examination of these open questions for solid solutions in the system $Pr_xCa_{1-x}MnO_3$ focussing in particular on the influence arising from oxygen deficiency. The results are not only discussed from the perspective of general interest but notably also in view on their eventual relevance for resistively switching thin film devices of PCMO. In this context the present work aims to contribute more specifically to a still ongoing controversial discussion [78-86] about the exact influence of oxygen vacancies on resistive contributions during switching in PCMO-related devices. Several individual model concepts ranging from polaronic electric transport [79-82], the suggestion of localized Mott-transitions [83] induced by oxygen deficiency, indications on the role of strongly correlated electrons [85-86], up to the proposition of a modulated insulating tunnel barrier at the electrode interface of PCMO are so far projected in literature. Regarding electric transport, the question whether the charge carrier concentration or mobility in oxygen deficient PCMO prevails is still open, however. With respect to subtle chemical changes occurring at the electrode interface upon motion of oxygen vacancies, the reported details on their concentration and redistribution seem to be yet insufficient for a really cohesive understanding.

2. Experimental

2.1. Powder synthesis and ceramic processing

Powders with six different Pr:Ca-ratios covering the entire compositional range of solid solutions $Pr_xCa_{1-x}MnO_3$ that are formed by the orthorhombic endmembers $CaMnO_3$ (space group *P m n a* [87]) and $PrMnO_3$ (space group *P b n m* [88]) were prepared by conventional solid-state reaction: x = 0.0, 0.1, 0.3, 0.5, 0.7, 0.9 and 1.0. Commercial grade powders of Pr_6O_{11} ($Pr_2O_3 \cdot 4PrO_2$), $CaCO_3$ and MnO_2 (Chempur. 99.9% purity) served as raw materials and were weighed in appropriate proportions. Intensively blended powder mixtures were homogenised and ball-milled in 2-Propanol for 6 h using beads (∅ 2 mm & 3 mm) of partially stabilized zirconia (YTZ, Tosoh Corporation).

After milling the resulting slurries were dried using a rotary evaporator (Rotavapor R-134, Büchi Labortechnik) and calcined in air for 2 h in a muffle furnace (Nabertherm GmbH) at 950°C in the case of phase pure $PrMnO_3$ (x = 1) and at 1200°C for all other, Ca-containing compositions (x = 0 to 0.9). The as-calcined powders were fine-milled again, for 6 h in 2-Propanol by ball-milling using YTZ-beads and finally dried. Particle size distributions were verified with a laser diffraction particle analyser (Mastersizer, Malvern Instruments GmbH), and averaged out at approximately 1 μm, always.

Finally, the as synthesised powders were firmly brought together with 3 wt.-% of binder (Optapix PAF 35, Zschirmer & Schwarz GmbH Co. KG) in an agate mortar, uniaxially pelletized in a steel die (∅ 12 mm) with a pressure of 200 MPa and further compacted by cold isostatic pressing at 750 MPa for several minutes.

Before sintering these green bodies were decarbonised for 12 h at 600°C in air in order to completely remove all eventual residues originating from binder addition. All pellets pre-consolidated in this way were sintered for 6 h at 1350°C in a gas tight Al_2O_3 tube furnace under flowing pure oxygen O_2 and cooled down to room temperature at a rate of or below 1 K/min in order to prevent crack-formation.

2.2. Microstructural and crystallographic characterization

The Archimedes method was used to measure densities of sintered ceramic pellets. Microstructural examinations were carried out on polished and thermally etched cross sectional specimens using scanning electron microscopy (SU-8000, Hitachi) and the average grain-size was evaluated according to the line intercept method [89]. Powder X-ray diffraction patterns were recorded (RINT-2500, CuK_α-radiation, λ = 154.05 pm, Rigaku Corporation) on crushed, finely ground sintered ceramic samples to study phase compositions, crystal structures and lattice parameter. Pawley's method [90] was used to compute the lattice parameter from diffraction data. Crystallographic studies on partially reduced ceramic samples were carried out using synchrotron- (Aichi Synchrotron Radiation Center, BL5S2, λ = 68.89 pm, 1.8 keV) and neutron-diffraction (Ibaraki J-Parc, iMATERIA, BL20).

2.3. Analytical characterization and iodometry

The cationic stoichiometries of as sintered pellets were verified by combined analytical determinations using ICP-OES (Inductively coupled plasma – optical emission spectrometry, iCAP6000, Thermo Fischer Science) and XRF (X-ray fluorescence analysis, ZSX, Rigaku Corporation) on crushed ceramic specimens.

Redox titration based on iodometry, refer to e.g. [91], was used to quantify the amounts of manganese in the different valence states (Mn^{3+} and Mn^{4+}) and to calculate the oxygen content in the different oxide compositions, correspondingly. For this purpose, approximately 150 mg of a respective crushed sintered pellet were weight in a flask and dissolved in a mixture consisting of 30 ml aqueous potassium iodide solution (0.5 M) and of 50 ml concentrated hydrochloric acid (Merck, 25%). The initial potassium iodide solution was prepared from reagent grade KI (Sigma- Aldrich, 99.0%) and degassed, nearly oxygen-free, distilled water in order to prevent side reactions during iodometric titration and to minimize systematic errors during the determination of the valence states of Mn. Therefore, purified high-grade argon was bubbled overnight at room temperature through the used quantity of distilled water. Consequently, also hydrochloric acid was degassed before utilization in the same way. All further analytical steps of the titration were carried out under a protective atmosphere of purified flowing argon.

Upon dissolution higher valent cations of manganese, are reduced to divalent Mn^{2+} by I^- resulting in the release of iodine I_2, according to equations (1) and (2):

$$2Mn^{3+} + 2I^- \rightarrow Mn^{2+} + I_2 \quad (1)$$

$$Mn^{4+} + 2I^- \rightarrow Mn^{2+} + I_2 \quad (2)$$

After completely dissolving the solid analyte the cooled off solution was titrated with a standardized solution of sodium thiosulfate, $Na_2S_2O_3$ (Sigma-Aldrich, 0.05 M) using starch as an indicator. During this additional redox reaction iodine I_2 is reduced back to iodide ions I^- and the thiosulfate ions are oxidized to tetrathionate ions according to equation (3):

$$I_2 + 2S_2O_3^{2-} \rightarrow 2I^- + S_4O_6^{2-} \quad (3)$$

Several blank measurements were conducted on a daily basis and all titration results were corrected in order to compensate the influence of oxidized iodide ions through unavoidable small concentrations of the oxygen present in the solvents. Finally, the amounts of manganese in the different oxidation states and the average valence state α of manganese as well as the deficiency or excess in oxygen stoichiometry were calculated assuming that the valence states of praseodymium Pr^{3+}, of calcium Ca^{2+} and of oxygen O^{2-} are constant, respectively.

Conclusively, in order to monitor and evaluate the progress of reduction, the degree of non-stoichiometry δ regarding the content of oxygen upon thermal reduction in the solid solution system $Pr_xCa_{1-x}Mn^{\alpha+}O_{3\pm\delta}$, where the value α represents the average valence of Mn ($3 \leq \alpha \leq 4$), was determined using thermogravimetric measurements (STA 429 Netzsch Gerätebau GmbH, heating and cooling rates: 5 K/min) up to temperatures of 1100°C at most.

These experiments were carried out in gaseous mixtures of either 20 vol.-% O_2 in Ar ("synthetic air") or of argon with decreasing but constant levels of the partial pressure of oxygen $p(O_2)$.

2.4. Determination of electrical transport properties

2.4.1. Electrical DC-conductivity

Electrical DC-conductivity σ was measured in dependence of temperature and partial pressure of oxygen $p(O_2)$ using a four-probe method. Rectangular rods of 10 mm in length, 5 mm in width and 1 mm in thickness were cut out of originally cylindrically shaped as sintered pellets with a diamond wire saw. Four Pt-electrodes were applied by sputtering in a fixed distance from each other. Around each of these contact points a 100 µm thick Pt-wire was firmly twisted in order to ensure a mechanically stable electric connection, respectively.

Both outer contacts were connected to a current source (6220, Keithley Instruments) and the two inner electrodes to a digital voltmeter (PM2534, Philips) in order to record the corresponding voltage drop arising from the applied current. The conductivity σ of each specimen under consideration was calculated from the linear (ohmic) relationship between voltage drop and applied current as well as from the respective geometrical dimensions of the sample.

The influence of the thermodynamic parameter temperature and partial pressure of oxygen $p(O_2)$ on conductivity were systematically explored: temperature dependence of conductivity was determined in "synthetic air" (Ar + 20 vol.-% O_2) from room temperature up to 1000°C, whereas the effect of the partial pressure of oxygen $p(O_2)$ was studied in the range from 1 atm down to 10^{-15} atm at 750°C and 900°C, respectively. For this purpose, an in house installed experimental setup consisting of a gas-tight quartz-glass tube furnace connected to an oxygen pump (SEMG5, Zirox GmbH) and to a gas-mixture system has been used. Reliable values of the partial pressure of oxygen $p(O_2)$ were realized with this setup in combination with humidified gas mixtures of hydrogen H_2, oxygen O_2 and Argon Ar saturated with water H_2O in appropriate mixing ratios. At the outlet of the heated quartz-glass tube the $p(O_2)$ was monitored using an oxygen sensor (Electrolysis cell 10/006-01/00, Zirox GmbH).

2.4.2. Thermopower and Seebeck-coefficient

The experimental determination of the thermopower for the evaluation of the corresponding Seebeck-coefficient S has been carried out using a commercial thermoelectric measurement system (RZ2001, Ozawa Science Co., Ltd.). Rod-type specimens of 10 mm in length, 5 mm in width and 1 mm in thickness were cut from cylindrically shaped sintered ceramic pellets and used as samples. The resulting rectangular bar specimens were subsequently sandwiched between two probes of the measurement system containing Pt-electrodes as electric contacts and R-type thermocouples for recording temperatures.

The Seebeck-coefficients were calculated from the linear increase of the thermoelectromotive force resulting from a given, applied temperature gradient along the sample. All measurements were carried out in air and the temperature was tuned from 50°C up to 1000°C. Below 50°C no steady-state temperature gradient could be realized.

3. Results and Discussion

3.1. Densification behaviour and structural evolution

Figure 1 represents the temperature dependence of electrical DC-resistivity for phase-pure $CaMnO_3$ ceramics, one endmember of the solid-solutions of the present study.

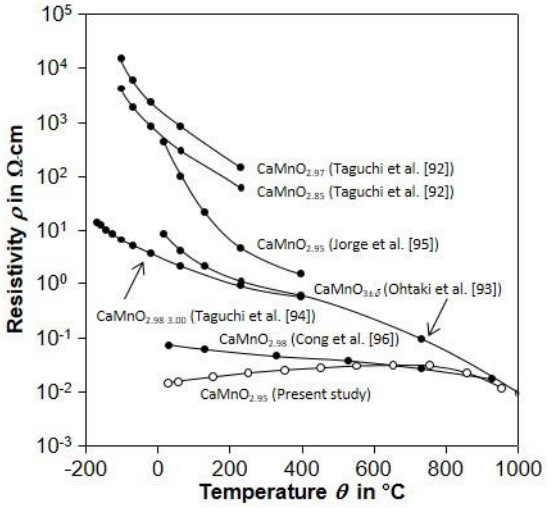

Figure 1: Temperature dependence of electric DC-conductivity in air for phase-pure $CaMnO_{3\pm\delta}$. Full symbols (●) represent data reported in literature earlier [92-96] and open symbols (○) own measurements, respectively.

The data displayed have been taken from several different former reports published earlier [92-96] and are compared to own results obtained for an almost fully oxidized and densified ceramic specimen of $CaMnO_{2.95}$.

Conductivity values of earlier studies shown in Figure 1 obviously reveal for practically all cases that the own phase pure composition of $CaMnO_{2.95}$ is significantly less insulating: The maximum difference in resistivity may extent up to 5 orders of magnitude at room temperature, for instance. At the same time a substantial and unsystematic spread of already published data can be recognized when comparing these different studies. This extensive scatter suggests a strong influence on material preparation or microstructure. A systematic variation with the degree of oxygen deficiency cannot be identified.

In contrast to own results, the temperature coefficient of resistivity is negative, whereas the present study shows, that up to about 700°C resistivity increases with temperature indicating metallic-like conductivity behaviour and then decreases at more elevated values, which is typical for semiconducting materials.

In conclusion, all these considerable discrepancies observed for one and the same even relatively simple composition of $CaMnO_3$ prompted the authors of the present study to devote particular care regarding ceramic processing in order to ensure a sufficiently reliable and reproducible sample quality for a systematic study on the defect chemistry and electric transport properties in the solid-solution system $Pr_xCa_{1-x}MnO_3$.

Compositions based on the compound $CaMnO_3$ turned out to require a calcination temperature of at least 1200°C to ensure full thermal reduction of MnO_2 and to prevent secondary phases such as for instance Ca_2MnO_4. Because stoichiometric $CaMnO_3$ undergoes a series of phase transitions upon heating or subsequent cooling [97, 98], equation (4), going along with the release of oxygen and thus with the reduction of Mn a careful adjustment of the sintering scheme seemed to be necessary to ensure a defined initial oxidation state of all ceramics.

$$\text{Orthorhombic} \underset{890°C}{\overset{896°C}{\rightleftharpoons}} \text{Tetragonal} \underset{908°C}{\overset{913°C}{\rightleftharpoons}} \text{Cubic} \qquad (4)$$

Therefore, sintering treatments were exclusively carried out in pure oxygen O_2.

Leonidova et al. [98] observed that the transition temperatures specified in equation (4) shift to higher values if the partial pressure of oxygen $p(O_2)$ is enhanced.

Own dilatometric examinations detected, that $CaMnO_3$ pellets indeed reveal an abrupt expansion in thickness by about 0.7% upon cooling (5 K/min) after in-situ sintering at 1350°C for 6 h in air. This dilatation appears at around 800°C in atmospheric air. The effect appears to be related to a strong increase of the thermal expansion coefficient at about 900°C [98] arising from the phase transitions when oxygen deficient $CaMnO_{3-\delta}$ is cooled down from higher temperatures and possibly re-oxidized. Ceramic pellets already densified at elevated temperatures accumulate unrelaxed mechanical internal strains upon cooling finally resulting in possible cracking. For this reason, the cooling rates after oxidizing sintering of all compositions reported here were reduced to 1 K/min or even to lower values.

As a result, highly densified and crack-free ceramics were obtained, as outlined in Figure 2. Comparing the polished surfaces of the internal central planes shown in Figure 2(a) and (b) clearly demonstrates that sintering at a high partial pressure of oxygen in combination with extremely slow cooling results in virtually crack-free ceramics. Possibly, former studies [92-96] ignored the eventual presence of internally formed flaws and neglected the possibility of significantly larger values of insulation resistance obtained upon experimental determination resulting from cracking, as presented in Figure 1.

Representative examples for the microstructures of as-sintered $Pr_{1-x}Ca_xMnO_{3\pm\delta}$ ceramics are shown in Figure 3 and illustrate highly densified and uniform grain structures obtained. The grain-size depends on the composition but not in a systematic way, as can be recognized from Table 1, where numerical values of densities and grain-sizes are summarized along with other analytical results that are described in more detail in section 3.3.

The measured densities for $Pr_xCa_{(1-x)}MnO_{3\pm\delta}$ ceramics obtained after adjusting the sintering procedure in the previously described manner follow in almost excellent agreement a linear relationship in dependence of the Pr-content x for the Ca-rich side up to approximately $x = 0.7$. Only very minor deviations from expected values that would be predicted theoretically [87, 88, 99-105] occur. Beyond the region up to a Pr-content of $x = 0.7$ the experimental densities still correspond to theoretical expectations but the slope of the originally linear increase flattens for compositions close to pure $PrMnO_3$.

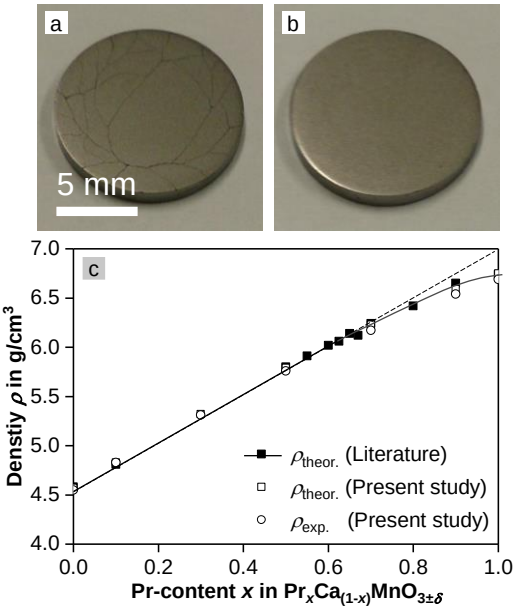

Figure 2: Densification behaviour of $Pr_xCa_{(1-x)}MnO_{3\pm\delta}$ ceramics upon sintering.
(a) $CaMnO_3$ ($x = 0$) sintered at 1350°C in synthetic air (Ar + 20 vol.-% O_2) and cooled at a rate of 1 K/min. The polished internal face in the centre of the pellet reveals cracks.
(b) $CaMnO_3$ ($x = 0$) sintered at 1350°C in pure oxygen O_2 and cooled at a rate of 0.25 K/min. No cracks are visible, even not in the interior of the sintered pellet.
(c) Dependence of measured (open circles ○) and theoretical density from composition. The values of theoretical density were taken from literature (closed squares, ■) [87, 88, 99-105] or derived from own refined X-ray diffraction patterns (open squares, □)

Pr-containing ceramics tend to have a more refined microstructure compared to pure $CaMnO_3$, however no systematic influence of the Pr-content can be recognized. Except for phase pure $CaMnO_3$ and the composition $Pr_{0.7}Ca_{0.3}MnO_{3\pm\delta}$ all ceramics revealed an average grain-size around or well below 5 µm and the relative densities exceeded 99 % of the theoretical value, in general.

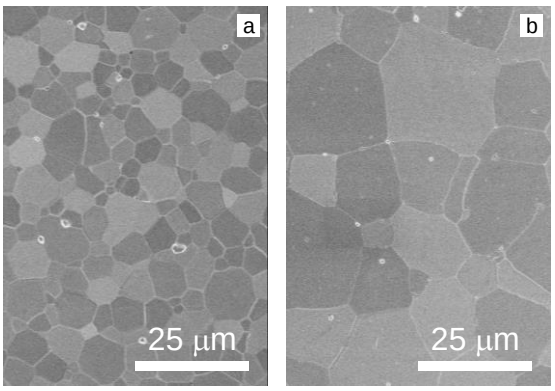

Figure 3: Microstructures of $Pr_xCa_{(1-x)}MnO_{3\pm\delta}$ ceramics, sintered at 1350°C in pure oxygen O_2. (a) $Pr_{0.50}Ca_{0.50}MnO_3$ ($x = 0.50$) and (b) $Pr_{0.70}Ca_{0.30}MnO_3$ ($x = 0.70$).

It is interesting to note, perhaps, that the already mentioned composition $Pr_{0.7}Ca_{0.3}MnO_{3\pm\delta}$ shows the lowest density (99%) and largest grain-size (14.6 µm), which may indicate that grain-growth processes, impeded volume-diffusion in favour of transport mechanisms favouring coarsening play a role. This purely speculative interpretation, however, has not been followed up in more detail.

Nominal Composition	Density ρ / g·cm^{-3}		Grain-size / µm	Stoichiometry ratios		Mn-valence α
x in $Pr_xCa_{1-x}MnO_{3\pm\delta}$	$\rho_{theor.}$	$\rho_{exp.}$		Pr : (Pr+Ca)	(Pr+Ca) : Mn	
0.0	4.57	4.55 (99.6%)	19.6	-	1.00(0)	3.94
0.1	4.83	4.83 (100%)	2.8	0.09(6)	1.00(0)	3.87
0.3	5.32	5.31 (99.8%)	1.8	0.28(9)	0.99(8)	3.68
0.5	5.79	5.76 (99.4%)	5.2	0.48(8)	0.99(5)	3.50
0.7	6.23	6.17 (99.0%)	14.6	0.69(2)	0.99(3)	3.32
0.9	6.59	6.54 (99.3%)	3.7	0.90(3)	1.00(2)	3.16
1.0	6.75	6.69 (99.2%)	3.6	-	1.00(2)	3.07

Table 1: Summarized overview on the numerical values regarding densities, grain-sizes, and analytical results with respect to the stoichiometric ratios (Pr-content x and A:B-ratio) as well as the average valence state of Mn-cations. The values of theoretical density were determined from the crystallographic parameter evaluated from XRD-measurements, those for the stoichiometric ratios by ICP- and XRF-analysis, insignificant figures being given in (brackets), and those for the valence state of Mn by iodometry.

3.2. Crystallographic structure

Only negligible traces of PrO_2 could be detected in very few cases for compositions being rich in Pr-content (x = 0.9 or x = 1.0).

Figure 4 represents the XRD diffraction patterns recorded for all ceramics examined in the present study. They could be indexed according to the orthorhombic space group *P m n a* up to a Pr-content x of 0.7. The corresponding lattice parameter a, b and c of the orthorhombic unit cell were refined using Pawley's method [90] and are shown including the unit cell volume V in Figure 5 in dependence of the Pr-content x.

The pseudo-cubic lattice ($a \approx b/\sqrt{2} \approx c$) expands linearly upon substitution of Ca^{2+}- by Pr^{3+}-cations up to a Pr-concentration $x=\left[Pr_{Ca}^{\bullet}\right]$ of approximately 70%. The rate of volume expansion per mol-% of Pr added is approximately three times larger than the value that would be expected from the difference of the ionic radii of Ca^{2+} and Pr^{3+}. Beyond a Pr-content x of 0.7, the volume of the orthorhombic unit cell increases even more steeply indicating a transition and reduction in symmetry from *P m n a* towards *P b n m*.

Obviously, this change in lattice symmetry is induced by an increasing reduction of manganese upon Pr-substitution for Ca on the A-site and an enhanced concentration of trivalent Mn^{3+}-cations at the expense of Mn^{4+}-cations that are considerably smaller in size.

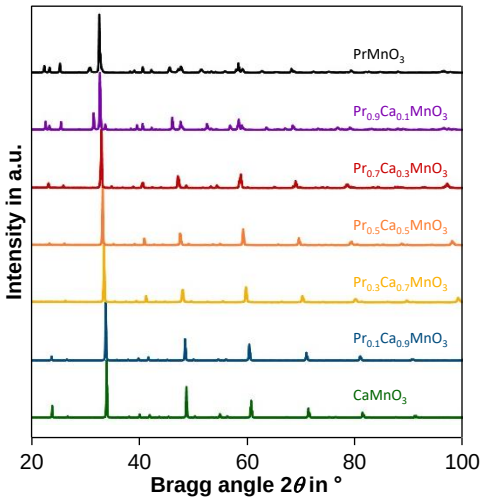

Figure 4: X-ray powder diffraction patterns recorded for sintered $Pr_xCa_{1-x}MnO_{3\pm\delta}$ ceramics with different Pr-content ranging from x = 0 ($CaMnO_3$) to x=1 ($PrMnO_3$).

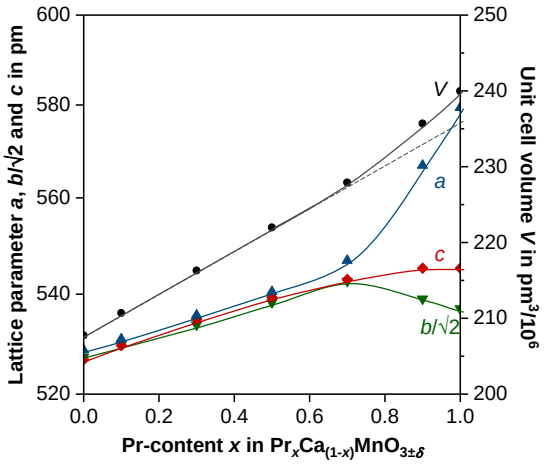

Figure 5: Lattice parameter a, b and c as well as the unit cell volume V for the orthorhombic solid solutions series $Pr_xCa_{1-x}MnO_{3\pm\delta}$. The results were obtained from refined diffraction patterns (Figure 4) recorded for ceramics with different Pr-contents x ranging from 0 ($CaMnO_3$) to 1 ($PrMnO_3$).

According to Shannon [106, 107] the atomic radii of Mn-cations in octahedral coordination (CN=6) are $r(Mn^{3+})$ = 64.5 pm and $r(Mn^{4+})$ = 53 pm, whereas the cationic radii of Ca^{2+} and Pr^{3+} in cuboctahedral coordination (CN=12) are relatively similar: $r(Ca^{2+})$ =134 pm and $r(Pr^{3+})$ =137 pm.

Obviously, this change in lattice symmetry is induced by an increasing reduction of manganese upon Pr-substitution for Ca on the A-site and an enhanced concentration of trivalent Mn^{3+}-cations at the expense of Mn^{4+}-cations that are considerably smaller in size. According to Shannon [106, 107] the atomic radii of Mn-cations in octahedral coordination (CN=6) are $r(Mn^{3+})$ = 64.5 pm and $r(Mn^{4+})$ = 53 pm, whereas the cationic radii of Ca^{2+} and Pr^{3+} in cuboctahedral coordination (CN=12) are relatively similar: $r(Ca^{2+})$ =134 pm and $r(Pr^{3+})$ =137 pm.

Considering the different experimental valence states (Table 1) and radii of Mn-cations the tolerance factor t [108] of the perovskite unit cell continuously decreases from an almost ideal value of t =1.00 for pure $CaMnO_3$ down to t = 0.96 for $PrMnO_3$ with increasing Pr-content. This indicates that MnO_6-octahedra gradually require more space than the available room provided by the surrounding cubic cage formed by A-site cations. In consequence octahedral tilting or rotation may occur resulting in the observed reduction of crystallographic symmetry. Moreover, the Jahn-Teller effect is thought to contribute to the observed lattice distortion, too. In consequence, the lattice expands considerably in the a-direction <1 0 0>, whereas the b-axis becomes shorter and while the c-axis virtually remains constant on the Pr-rich side of the system $Pr_xCa_{(1-x)}MnO_{3\pm\delta}$ when x increases.

3.3. Chemical analyses and the pristine valence state of Mn

Analytical results regarding stoichiometry on the cationic sites of the perovskite listed in Table 1 confirm, that the degree of Ca-substitution x and the compositional ratio of both A-site cations, Ca^{2+} and Pr^{3+}, relative to the B-site cations of Mn essentially correspond to the initial nominal values.

Figure 6 shows the average valence state α of $Mn^{\alpha+}$-cations, located on the B-site, and correspondingly the derived nonstoichiomentry with regard to oxygen in dependence of the substitutional degree x in ceramics of the solid solution system $Pr_xCa_{(1-x)}MnO_{3\pm\delta}$ sintered in pure oxygen. Even after sintering in 100% O_2 at atmospheric pressure pure $CaMnO_3$-ceramics ($x = 0$) contain about 6 mol-% of trivalent cations Mn^{3+} that have to be compensated electrically by vacancies of oxygen $V_O^{\bullet\bullet}$:

$$\left[V_O^{\bullet\bullet}\right] = \frac{1}{2}\left[Mn'_{Mn}\right] \qquad (5)$$

This regime of oxygen deficiency (red area in Figure 6(b)) extends to a Pr-content x of exactly 0.5, where the numbers of trivalent and tetravalent cations of Mn are completely balanced. At larger degrees of substitutions $x > 0.5$ of Ca^{2+} by Pr^{3+} the concentration of reduced, trivalent Mn^{3+} surpasses the one of tetravalent Mn^{4+} and consequently the formation of metal vacancies can be expected (blue area in Figure 6(b)) upon sintering under oxidizing conditions. In fact, very minor traces of – possibly expelled – PrO_2 could be detected by careful inspection through XRD for the compositions with $x = 0.9$ and $x = 1.0$.

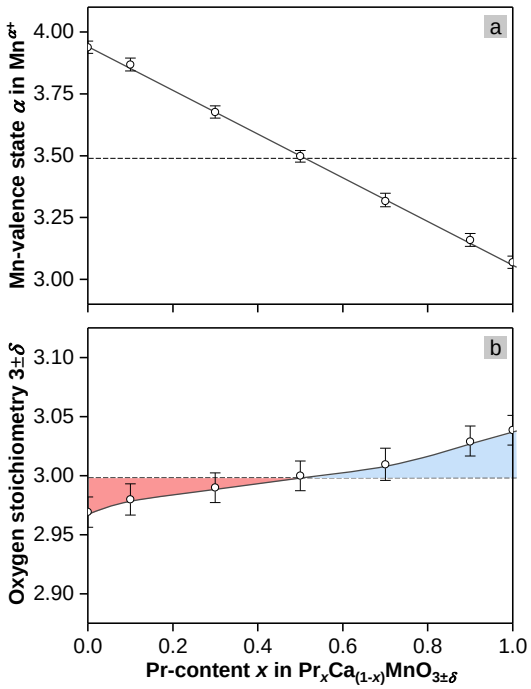

Figure 6: Analytical results obtained by Iodometry in dependence of the Pr-content x: (a) average valence state α of $Mn^{\alpha+}$-cations and (b) oxygen stoichiometry $3\pm\delta$.

Between both end-members of the present solid-solution series, $CaMnO_3$ ($x = 0$) and $PrMnO_3$ ($x = 1$) the average value of the Mn-valence almost ideally follows a linear relationship. This behaviour is in good agreement with the observations, how crystallography develops in this system with increasing content of Pr^{3+} substituting Ca^{2+} (Figure 5).

It should be noted, that iodometric titrations carried out for determining the average Mn-valence state α^+ have been conducted several times. They were highly reproducible and resulted in a standard deviation of 0.026 only.

3.4. Thermal reduction behaviour

Thermogravimetric analyses of the thermal reduction behaviour in "synthetic air" (Ar + 20 vol.-% O_2) revealed the evolution of oxygen nonstoichiometry from the pristine state after sintering in pure oxygen upon further heating and cooling in dependence of the materials compositions, as shown in Figure 7. Phase pure $CaMnO_3$ remains relatively stable keeping a constant deficiency of oxygen of about $\left[V_O^{\bullet\bullet}\right] = 0.01$ up to a temperature of approximately 750°C, upon heating. Then, on further increase of temperature, oxygen is gradually released from the lattice resulting in a composition of about $CaMnO_{2.80}$ at 1100°C. The loss in oxygen is also influenced by the before mentioned phase transitions from the orthorhombic to a tetragonal and finally cubic modification at around 900°C and appears to be essentially reversible upon cooling. However, the uptake of oxygen almost back to the original pristine condition upon temperature reduction seems to be kinetically delayed resulting in an overall hysteretic kind of thermal redox-behaviour. Upon substitution of Ca^{2+} by Pr^{3+} in $Pr_xCa_{(1-x)}MnO_{3\pm\delta}$ the onset of oxygen release is shifted to higher temperatures and the total amount of oxygen vacancies formed at the maximum temperature of 1100°C is reduced. At the same time the extent of the hysteretic delay in oxygen uptake upon cooling becomes smaller.

According to the previously presented results shown in Figure 6 thermal reduction can be expressed as defect chemical reaction equation (6):

$$2Mn_{Mn}^{\times} + 6O_O^{\times} \rightleftharpoons 2Mn'_{Mn} + V_O^{\bullet\bullet} + 5O_O^{\times} + \frac{1}{2}O_2^{(g)} \qquad (6)$$

Apparently, the addition of Pr strongly enhances the reduction resistance in solid solutions of the system $Pr_xCa_{(1-x)}MnO_{3\pm\delta}$ and compositions with a Pr-content x above 0.5 almost retain their original level of oxygen stoichiometry upon thermal cycling.

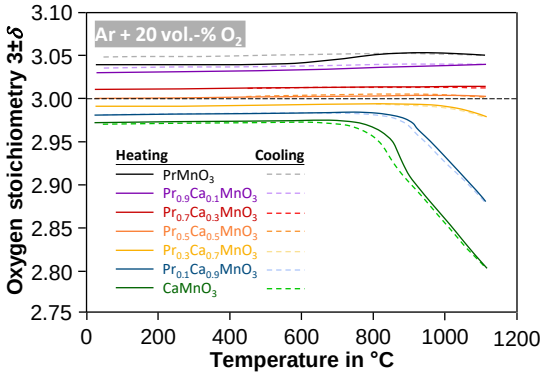

Figure 7: Thermogravimetric determination of oxygen-nonstoichiometry upon thermal reduction for different compositions $Pr_xCa_{1-x}MnO_{3\pm\delta}$ ($x = 0$, 0.1, 0.3, 0.5, 0.7, 0.9 and 1.0). Full lines represent the heating cycle and broken lines the cooling cycle.

3.5. Reduction behaviour upon lowering $p(O_2)$

Figure 8(a) represents the dependence of oxygen stoichiometry at elevated temperatures and reduced partial pressures of oxygen for several selected ceramic compositions determined by thermogravimetric analysis (TGA).

Results obtained by ex-situ reduction experiments for the particular case of $Pr_{0.7}Ca_{0.3}MnO_{3\pm\delta}$ are included too. These are referred to again in more detail in section 3.7.

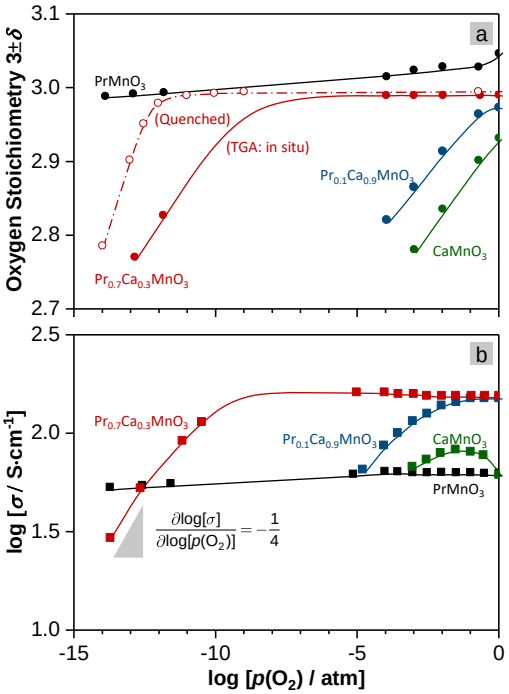

Figure 8: Dependence of (a) oxygen nonstoichiometry and (b) DC-conductivity σ on partial pressure of oxygen $p(O_2)$ for different compositions $Pr_xCa_{1-x}MnO_{3\pm\delta}$ (x = 0.0, 0.1, 0.7 and 1.0). All experimental results refer to a measurement temperature of 950°C. Full lines in Figure 8(a) represent thermogravimetric analyses and the dashed line ex-situ experiments for the composition $Pr_{0.7}Ca_{0.3}MnO_{3\pm\delta}$ where oxygen deficiency was determined by iodometry after quenching ceramic specimens annealed at 950°C and at various partial pressures of oxygen.

Upon reduction at 950°C, the compound $CaMnO_3$ shows a continuous loss in mass of about 5% due to the release of oxygen from the lattice up to a maximum total deficiency of almost 7.5% at $p(O_2) = 10^{-3}$ atm before decomposition.

The value $\delta \approx -0.1$ of oxygen deficiency obtained here at $p(O_2) \approx 0.2$ ("synthetic air") corresponds well with other TGA-measurements revealing thermal reduction in Ar + 20 vol.-%, shown in figure 8.

In the case of Pr-containing compositions the onset of losses in lattice oxygen and thus of ionic compensation upon reduction is retarded towards lower partial pressures of oxygen. For $Pr_{0.1}Ca_{0.9}MnO_{3\pm\delta}$ the original pristine deficiency in oxygen is almost retained down to $p(O_2) \approx 0.2$ atm ("synthetic air"): $\delta \approx -0.03$; this value is also in good agreement with previous TGA-experiments upon thermal reduction (Figure 8). At a Pr-content of $x = 0.7$ massive oxygen vacancy formation upon reduction during TGA seems to start around $p(O_2) \approx 10^{-9}$ atm. Sintered specimens of this latter composition that were reduced ex-situ, subsequently quenched and then analysed using iodometry reveal a large reduction in oxygen-content (ca. 7%) at a partial pressure of oxygen about three orders of magnitude below the transition point extrapolated from TGA. This experimental discrepancy may have resulted from different equilibration conditions and are not thought to arise from practical inaccuracies related to the measurements. Finally, phase pure $PrMnO_3$ reveals a comparatively moderate reduction of mass loss (≈ 2%) upon reduction only.

In conclusion, TGA experiments provided first indications about the reduction behaviour and about the formation of oxygen vacancies in the solid solution system $Pr_xCa_{(1-x)}MnO_{3\pm\delta}$. A more refined crystal chemical examination regarding the specific composition $Pr_{0.7}Ca_{0.3}MnO_{3\pm\delta}$ is presented and discussed in section 3.7. in context with concentrations and mobilities of electronic charge carriers and their quantitative dependence on oxygen-deficiency.

Figure 8(b) shows in analogy to the analytical results obtained from TGA and iodometry, how DC-conductivity is affected by reduction at 950°C. Qualitatively, similar trends as already observed with regard to oxygen nonstoichiometry can be noticed here. In the case of phase pure $CaMnO_3$ containing no additions of Pr, conductivity increases first with decreasing partial pressure of oxygen $p(O_2)$ down to approximately $3 \cdot 10^{-2}$ atm before falling off again upon further reduction. This intrinsic effect is obviously related to the enhanced reduction of originally tetravalent cations Mn^{4+} into trivalent cations Mn^{3+} increasing the concentration of mobile electronic charge carriers that contribute to small polaron hopping at elevated temperatures in this compound. Beyond this maximum of conductivity, the concentration of Mn^{4+} decreases until it vanishes completely and $CaMnO_3$ decomposes into compounds such as $CaMn_2O_4$ containing trivalent Mn-cations only. The initial conductivity levels at 950°C for both the Pr-containing compositions $Pr_{0.1}Ca_{0.7}MnO_{3\pm\delta}$ and $Pr_{0.7}Ca_{0.3}MnO_{3\pm\delta}$ in the original pristine condition after sintering in pure oxygen are comparable (≈ 150 S/cm). However, they are larger than the one for pure $CaMnO_3$ because of mixed valence states α of Mn-cations: $\alpha = 3.87$ ($x = 0.1$) and $\alpha = 3.32$ ($x = 0.7$). Upon reducing the partial pressure of oxygen $p(O_2)$ conductivity gradually decreases. However, the latter, Pr-richer composition ($x = 0.7$) retains its initial conductivity at an almost constant level, as might be expected from TGA results presented in Figure 8(a) down to a partial pressure of around $p(O_2) \approx 10^{-9}$ atm. In this regime a plateau of electronic compensation apparently prevails and only below $p(O_2) \approx 10^{-9}$ atm ionic compensation due to the formation of oxygen vacancies dominates the defect chemical situation.

In fact, under strongly reducing conditions ($p(O_2) < 10^{-12}$ atm) the slope of $\log[\sigma]$ versus $\log[p(O_2)]$ approaches a value of – ¼ being typical for the release of oxygen from the lattice, as can be recognized from equations (7) and (8):

$$2Mn_{Mn}^{\times} + O_O^{\times} \rightleftharpoons 2Mn_{Mn}' + V_O^{\bullet\bullet} + \frac{1}{2}O_2^{(g)} \qquad (7)$$

$$\left[Mn_{Mn}'\right] \sim p\,O_2^{\;-\frac{1}{4}} \cdot \left[V_O^{\bullet\bullet}\right] \qquad (8)$$

Generally, it can be concluded that the introduction of Pr^{3+}-cations into $CaMnO_3$ results in a considerable enhancement of reduction resistance with respect to the formation of oxygen vacancies $V_O^{\bullet\bullet}$. In a relatively extended region of partial pressures of oxygen $p(O_2)$ electronic compensation prevails. Strongly reduced compositions, where significant amounts of lattice oxygen are released, reveal a substantial decrease in electrical conductivity, because conductive paths for polaron hopping from Mn^{3+} to Mn^{4+} might be disrupted if intermediate oxygen sites in the perovskite structure are unoccupied, e.g. [68]. In principle the dependence of oxygen-nonstoichiometry and DC-conductivity on the partial pressure of oxygen $p(O_2)$ follow the same trend as the one reported for the system $La_xSr_{(1-x)}MnO_3$ [65-67, 73, 74, 76, 77]. Equally levels of oxygen deficiency as well as those of electric conductivity determined in the present study are comparable with results reported in the references mentioned.

However, most the data referred to in these citations are limited to compositions with a maximum alkaline earth metal content of 20%, only.

3.6. Electric conduction behaviour in the oxidized state

Before examining the electric conduction behaviour for the composition $Pr_{0.7}Ca_{0.3}MnO_{3\pm\delta}$ in detail with respect to the influence of oxygen-deficiency, a general survey on the overall system seemed to be necessary too: no systematic report has been reported so far in literature. Figure 9 represents the temperature dependence of the DC-conductivity for all compositions studied.

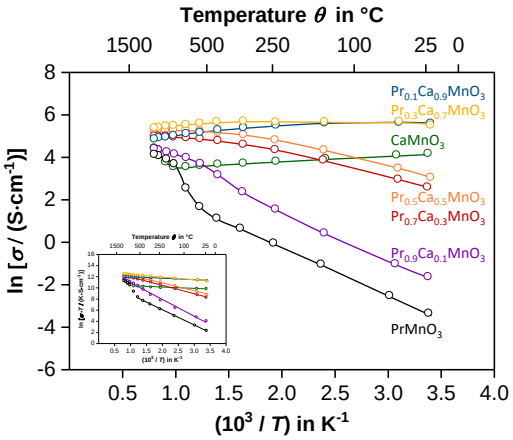

Figure 9: Temperature dependence of DC-conductivity in air for ceramics of different compositions $Pr_xCa_{1-x}MnO_{3\pm\delta}$ (x = 0, 0.1, 0.3, 0.5, 0.7, 0.9 and 1.0) sintered in pure oxygen. The inset shows a representation of $\ln(\sigma T)$ versus the reciprocal temperature.

Unlike to many other typical semiconducting electronic ceramics a logarithmic representation of conductivity versus reciprocal temperature does not result in a simple and general linear relationship for the investigated compositions of the system $Pr_xCa_{(1-x)}MnO_{3\pm\delta}$.

Because the prevailing electronic conduction mechanism is believed to rely on thermally activated small polaron hopping [109] the usual formal representation of conductivity includes a temperature dependent pre-exponential factor:

$$\sigma\ T\ = \frac{\mathrm{A}}{T}\cdot\exp\left\{\frac{-E_\mathrm{a}}{\mathrm{k_B}\cdot T}\right\} \qquad (9)$$

The factor A in equation (9) denotes a temperature independent constant, T the absolute temperature, E_a the activation energy and k_B the Boltzmann-constant. A diagram representing $\ln(\sigma\cdot T)$ depending on reciprocal temperature is shown in the inset of Figure 9.

Conductivity of pure $CaMnO_{2.95}$ has already briefly been outlined in Figure 1 before: At temperatures below 700°C conductivity decreases with raising temperatures, above 700°C, however, semiconducting behaviour is observed. In this region of high temperatures, the material becomes more conductive again with increasing temperature and the activation energy obtained (68 meV) is in fair agreement with results from Goldyreva et al. [110], who conversely reported on rather low-density ceramics. Thermal reduction becomes increasingly significant at high temperatures, as has been seen in section 3.4. already. The formation of oxygen vacancies $V_O^{\bullet\bullet}$ along Mn'_{Mn} extensively determine the conductivity behaviour by small polaron hopping.

In contrast to pure $CaMnO_{2.95}$ a continuous decrease of conductivity with increasing temperature occurs over the entire region investigated for compositions with a relatively low level of Ca-substitution x. A transition to a high-temperature region of semiconductivity could not be observed but only metallic-type behaviour instead. At such low substitutional levels $\left[Pr_{Ca}^{\bullet}\right]$, e.g. in the case of the composition $Pr_{0.1}Ca_{0.9}MnO_{3\pm\delta}$, vacancies of oxygen $V_O^{\bullet\bullet}$ are easily formed – refer to Figures 6(b), 7 and 8(a) – and are even present in the pristine state after sintering in pure oxygen. Upon thermal reduction the concentration of vacant oxygen sites in the lattice exponentially increases with temperature in a way determined by the free Gibbs energy of reduction. This means, that an increase of temperature results in an enhancement of unoccupied oxygen sites that may act as "scattering" centres to electrical conduction. The electronic charge transfer between distant Mn^{3+} and Mn^{4+} is then impeded causing an increase of resistivity with temperature. Simultaneously, however, the total degree of conductivity is located at a higher level compared to pure $CaMnO_3$ due to a growing concentration $\left[Mn'_{Mn}\right]$ upon substitution of Ca^{2+} by Pr^{3+}. In summary, it is believed that the defect chemical situation at a low extent of extrinsic substitution reduces the mobility of electronic charge carriers although their concentration is enhanced.

For higher concentrations x of Pr (x > 0.3) the temperature characteristics of conductivity change to a non-metallic, semiconductor-type behaviour in the entire temperature range covered. Furthermore, conduction by thermally activated polaron hopping apparently becomes continuously impeded with increasing Pr-content: conductivities σ at room-temperature decrease from σ(x = 0.3) = 240 S/cm, to σ(x = 0.7) = 14 S/cm and down to σ(x = 0.9) = 0.2 S/cm. Activation energies E_a inversely increase with progressive substitution of Ca^{2+} by Pr^{3+}: E_a(x = 0.3) = 43 meV, to E_a(x = 0.7) = 128 meV and finally up to E_a(x = 0.9) = 259 meV. In consequence, at elevated temperatures (e.g. 1250°C) the conductivities of all compositions studied converge to a relatively narrow interval around 130 S/cm.

In order to gain a more detailed understanding of the electrical conduction mechanisms in solid-solutions of the system $Pr_xCa_{(1-x)}MnO_3$, thermoelectromotive force has been measured in dependence of temperature (Figure 10).

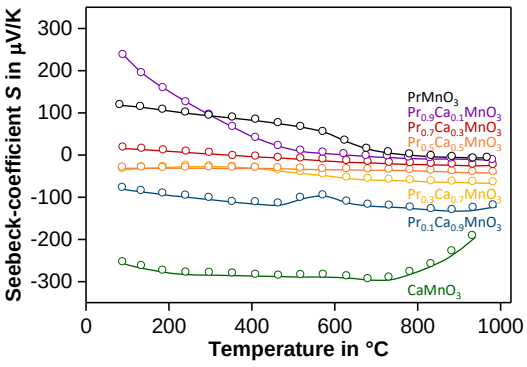

Figure 10: Temperature dependence of the Seebeck-coefficient measured in air for ceramics of different compositions $Pr_xCa_{1-x}MnO_{3\pm\delta}$ (x = 0.0, 0.1, 0.3, 0.5, 0.7, 0.9 and 1.0) sintered in pure oxygen.

Compositions relatively rich in Ca ($x \leq 0.5$) all revealed a negative Seebeck-coefficient irrespectively from the measurement temperature indicating overall n-type conduction. As can be recognized, the negative magnitude of the Seebeck-coefficient, however, becomes smaller when the Pr-content increases. Ceramics with a Pr-concentration with x = 0.9 or consisting of pure $PrMnO_3$ (not shown in Figure 10) even exhibit a positive Seebeck-coefficient and thus p-type conduction. Interestingly the composition $Pr_{0.7}Ca_{0.3}MnO_3$, a compound highly relevant for resistively switching devices, shows a very particular behaviour: at approximately 400°C a transition between p-type at lower temperatures and n-type conduction at higher

temperatures seems to occur. No conclusive interpretation for this change between electron- and hole-conduction is presented here. Neither the question, why this transition occurs around 400°C is addressed here. But it appears important to note, that in any case the magnitude of the thermoelectromotive force for this composition – being positive or negative – is the smallest observed in the present study. For this reason, the following section presents a more detailed examination of defect- and crystal-chemical aspects also related to the reduced state with regard to conduction behaviour for this particular composition.

3.7. Conductivity in oxygen-deficient $Pr_{0.7}Ca_{0.3}MnO_{3-\delta}$

Ceramic pellets with the composition $Pr_{0.7}Ca_{0.3}MnO_{3-\delta}$ and targeted levels of oxygen deficiency δ were prepared by annealing treatments at 950°C for 48 h at different partial pressures of oxygen $p(O_2)$.

$p(O_2)$ / atm	Oxygen nonstoichiometry	
	$(3-\delta)$	$\left[V_O^{\bullet\bullet}\right]$ / ‰
$10^{-0.7}$	2.997	1.0
$10^{-9.0}$	2.996	1.3
$10^{-10.0}$	2.993	2.3
$10^{-11.0}$	2.989	3.7
$10^{-12.0}$	2.979	7.0
$10^{-12.5}$	2.942	19.3
$10^{-13.0}$	2.902	32.7
$10^{-14.0}$	2.786	71.3

Table 2: Oxygen-deficiency in ex-situ reduced ceramics with the composition $Pr_{0.7}Ca_{0.3}MnO_{3\pm\delta}$ originally sintered in pure oxygen O_2.

After equilibration these specimens were quenched to room temperature at a rate of approximately 200 K/min and analysed by iodometry in order to evaluate the degree of oxygen nonstoichiometry, as presented in Table 2. Results of careful inspection regarding the phase compositions for selected specimens listed in Table 2 using laboratory and synchrotron XRD-measurements are shown in Figure 11. Enlarged views on the diffraction patterns obtained demonstrate, that phase pure perovskite compositions are only retained for a maximum level in oxygen nonstoichiometry $(3-\delta)$ of 2.979 ($\left[V_O^{\bullet\bullet}\right]$ = 7‰). Laboratory-scale XRD assessment (Figure 11(a)) did not turn out to be subtle enough to reveal this boundary of phase separation. For reducing conditions being more severe than $p(O_2) = 10^{-12}$ atm partial decomposition of the perovskite and formation of the secondary compound $Ca_2Mn_2O_4$ seem to be unavoidable at 950°C. Such specimens were not considered for further evaluations regarding electronic conduction, crystal- and defect-chemistry.

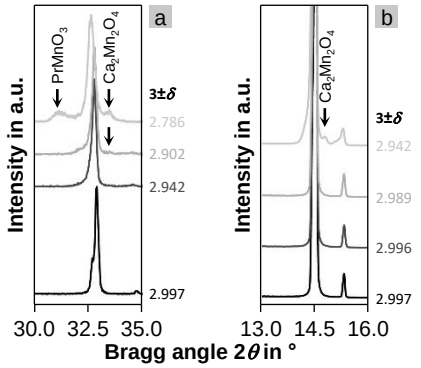

Figure 11: Laboratory and synchrotron inspection of phase decomposition for ex-situ reduced $Pr_{0.7}Ca_{0.3}MnO_{3-\delta}$ ceramics at different levels of oxygen deficiency.

One of the principal questions of the present study is, how the attained anionic deficiency in the oxygen sublattice of reduced compositions $Pr_{0.7}Ca_{0.3}MnO_{3-\delta}$ influences electronic conduction. Results presented in Figure 12(a) show, that conductivity at room temperature strongly decreases upon reduction by about one order of magnitude from about 25 S/cm ($Pr_{0.7}Ca_{0.3}MnO_{2.997;}$ $\left[V_O^{\bullet\bullet}\right]$ = 1.0‰) down to approximately 1.4 S/cm ($Pr_{0.7}Ca_{0.3}MnO_{2,979;}$ $\left[V_O^{\bullet\bullet}\right]$ = 7.0‰). At the same time the Seebeck-coefficient S increases from around 12 mV/K up to more than 30 mV/K.

Applying Heikes formula [111], equation (10), and the relation defining conductivity in terms of drifting elementary charge carriers, equation (11), both the concentrations c and mobilities μ of electronic charge carriers have been evaluated in dependence of oxygen deficiency, resulting in the representation shown in Figure 12(b).

$$S = \frac{k_B}{e} \cdot \ln\left\{\frac{4 - c \cdot V}{c \cdot V}\right\} \qquad (10)$$

$$\sigma = e \cdot \mu \cdot c \qquad (11)$$

In equation (10) k_B denotes the Boltzmann-constant, e the elementary charge and V the unit cell volume.

When oxygen from $Pr_{0.7}Ca_{0.3}MnO_3$ is extracted out of the lattice the concentration of charge carriers slightly decreases from about $8.1 \cdot 10^{-21}$ cm^{-3} to $7.3 \cdot 10^{-21}$ cm^{-3}. Simultaneously, the mobility, on the other hand, is drastically reduced from about $1.9 \cdot 10^{-2}$ cm^2/Vs down to $1.2 \cdot 10^{-3}$ cm^2/Vs when oxygen deficiency increases from 1.0‰ to 7.0‰.

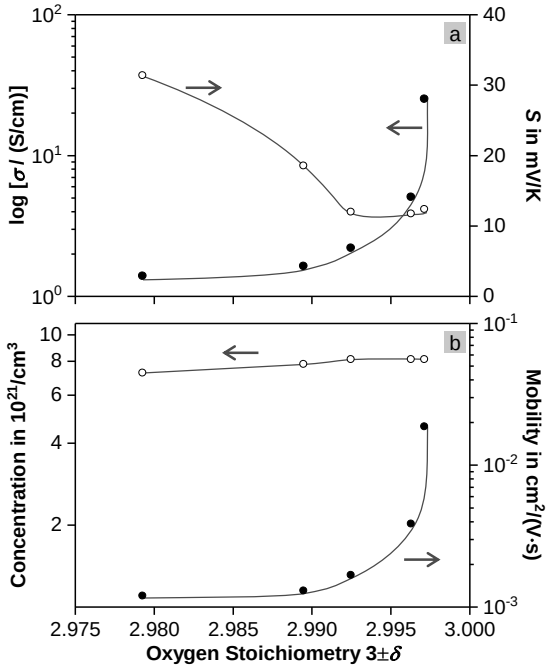

Figure 12: Dependence of (a) conductivity σ, the Seebeck-coefficient S – both measured at 25°C – (b) electronic charge concentration and mobility from oxygen stoichiometry.

It can therefore be concluded that the strong decrease of conductivity at room temperature in reduced $Pr_{0.7}Ca_{0.3}MnO_{3-\delta}$ is dominated by a hampered mobility of electronic charge carriers: Their concentration remains merely unaffected upon oxygen vacancy formation.

In order to understand the crystal-chemical mechanism of obstructed electronic transport upon the formation of vacant lattice sites of oxygen in reduced $Pr_{0.7}Ca_{0.3}MnO_{3-\delta}$ ceramics, refined neutron diffraction experiments were

carefully analysed with respect to the occupancy of the anionic sites in the perovskite structure. Rietveld refinements were carried out under the following conditions: (i) no constraints about the site occupancy of oxygen, (ii) assumption of an identical probability for oxygen being accommodated on O^1-sites at the aspices and O^2-sites in the basal plane of MnO_6-octahedra and finally (iii) fully occupied O^1-sites and vacancies supposed to form on the O^2-sites only. Figure 13 gives a schematic representation illustrating the arrangement of the different oxygen sites in the lattice.

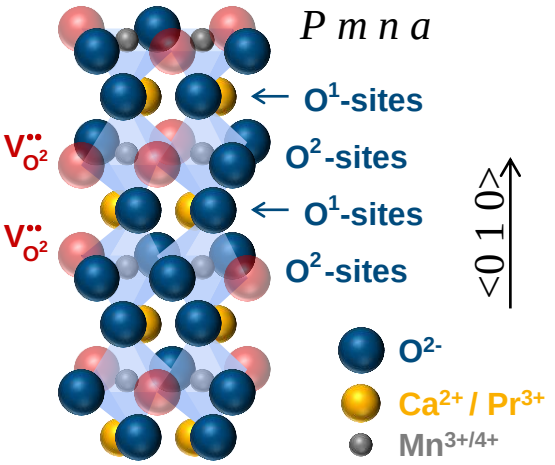

Figure 13: Crystal chemical model illustrating the arrangement of vacant and occupied oxygen lattice sites in reduced $Pr_{0.7}Ca_{0.3}MnO_{3-\delta}$ ceramics. Vacancies of oxygen are preferentially formed on O^2-sites of the lattice almost up to the level of phase decomposition upon reduction. The displayed relative proportion of unoccupied and regular oxygen sites is largely enhanced for the purpose of illustration.

As a result, the most reasonable descriptions (lowest R_{wp}-values) of the neutron diffraction data were obtained for the third scenario (iii), where oxygen vacancies are preferentially formed on the basal, equatorial lattice planes (0 ¼ 0) of MnO_6-octahedra in the orthorhombic lattice, or (0 ½ 0) planes in the cubic primitive unit cell, respectively, containing only one single formula unit of PCMO.

The occupancies for both lattice sites O^1 and O^2, the average bonding lengths b(Mn-O^1) and angles τ = ∢(Mn-O^1-Mn) are listed in Table 3 for a total a deficiency in oxygen $\left[V_O^{\bullet\bullet}\right]$ of 1.0‰, 1.3‰ and 3.7‰, respectively.

$\left[V_O^{\bullet\bullet}\right]$	(3 - δ)	$\left[O^1\right]$	$\left[O^2\right]$	b(Mn-O^1)	τ
1.0‰	2.997	1.000	0.993	196.15 pm	156.38°
1.3‰	2.996	1.000	0.989	196.23 pm	156.42°
3.7‰	2.993	1.000	0.982	196.31 pm	156.38°

Table 3: Occupancies for both lattice sites of oxygen O^1 and O^2, average bonding lengths b(Mn-O^1) and bonding angles τ in reduced $Pr_{0.7}Ca_{0.3}MnO_{3-\delta}$ ceramics for different levels of oxygen deficiency $\left[V_O^{\bullet\bullet}\right]$.

Most plausibly, according to these results from refined neutron diffraction patterns, oxygen vacancies $V_O^{\bullet\bullet}$ are formed on the O^2 lattice sites preferentially, while the sites O^1 are fully or almost fully occupied by oxygen anions O^2. In consequence, as outlined in the schematic representation in Figure 13, densely packed and "fully oxidized" lattice planes accommodating the A-site cations Ca^{2+} and Pr^{4+} are stacked between intermediate lattice planes located at (0 ¼ 0) being deficient in oxygen and hosting the trivalent and tetravalent manganese cations Mn^{3+} and Mn^{4+}. This kind of layered crystallographic structure can be regarded as a sort of "incomplete" superstructure. And this arrangement is thought to be responsible for the reduced mobility of elementary electronic charges during thermally activated small polaron hopping: Since most disrupted bonds between Mn-cations and O-anions are located in the oxygen deficient plane, electronic transport will favourably occur perpendicular to it in the crystallographic direction <0 1 0>. In the same way, also electrochemical migration of oxygen-anions O^{2-} could be affected by this anisotropic arrangement of oxygen-deficient and oxygen-rich crystallographic planes. The highest probability for ionic site exchange where O^{2-} anions hop into a vacant site or vice and versa would be along the direction <0 1 0> of the orthorhombic lattice.

Theoretical predictions based on model calculations and simulations [78] regarding the drift velocity for the electrically driven migration of oxygen anions in a conductive oxide separated from the contacting electrode through an oxide tunnel barrier assumed that the barrier height of the insulating barrier is tuned through the amount of oxygen present at the interface and concluded that the redistribution of oxygen during switching causes the change in resistance. Careful spectroscopic analyses applying hard X-ray photoelectron spectroscopy (HAXPES), EELS or impedance measurements of as deposited thin films or for different states of their electrical treatment upon switching [79-81] has been used to monitor the progress of the growth of the interfacial region at the electrode and of the chemical redox-reactions involved. The overall resistance of the total stack does not seem to be dominated by one single conduction mechanism but rather by a combination of several contributions [79-84], including both, an oxygen depleted zone within PCMO and an oxidized interface layer. It has been suggested, e.g. [82] that electronic inhomogenities imposed by electromigrative oxygen vacancy redistribution might cause the change in resistivity in oxygen deficient PCMO. But also competing tendencies between itinerant and localized states are discussed [85, 86].

The present work clearly evidences a direct relation between the level of oxygen deficiency in PCMO and electrical transport properties and shows that reduced mobility of charge carrier seems to be the dominant factor explaining the enhanced resistivity in the partially reduced condition and not their concentration. In contrast to other related materials systems the retarded charge carrier mobility already occurs readily at rather low concentrations of oxygen vacancies above 1000 ppm, realized already at relatively mild reducing conditions. For Lanthanum-doped Strontium-manganate ceramics, $La_{1-x}Sr_xMnO_3$, a similar drop of polaron mobility is only observed under very severe reducing conditions with $p(O_2)$ as low as 10^{-12} atm or below [67].

4. Conclusions

Oxygen deficiency in the solid-solution system $Pr_{(1-x)}Ca_xMnO_{3\pm\delta}$ strongly affects the electric conduction behaviour of reduced ceramics, initially sintered under defined, oxidizing conditions. The careful inspection of charge carrier concentration, mobility, concentration of vacancies of oxygen and crystallographic structure for the composition $Pr_{0.7}Ca_{0.3}MnO_3$ suggests the presence of a "incomplete" superstructure in which unoccupied oxygen sites are not randomly distributed but rather preferentially formed in the equatorial plane of MnO_6-octahedra, resulting in a "layered" distribution of oxygen-rich crystallographic planes alternating with oxygen-deficient ones along the direction <0 1 0> of the orthorhombic lattice. This arrangement could eventually also have a considerable effect on the oxygen transport along this crystallographic

orientation and thus on the formation of insulation transition layers in resistively switching thin film devices of this composition. It is interesting to note, that the findings of the present study are consistent with in-situ observations by integrated probe and transmission electron microscopy (TEM) reported by Liao et al. [112], who identified the formation of stripe-like domains associated with existing oxygen vacancies.

In their experimental setup these authors imaged the appearance of field induced striped patterns along one of the "pseudocubic" axes of the primitive unit cell upon switching resistivity in PCMO at an interface to a tungsten tip within the TEM.

Whether crystallographic distortions arising from elongated Mn-O[1] bonding lengths – bonding angles remaining merely unaffected – through the release of oxygen from the lattice, as they have been examined in the present study too, also influence the switching behaviour has to be clarified yet. Anyhow, electric conduction just beneath the actively switching transition layer will certainly be affected through interrupted ionic rows between Mn^{3+} and Mn^{4+}-cations, where oxygen anions O^{2-} are preferentially missing on (0 ¼ 0)-planes. Detailed analysis on systematically reduced and oxidized PCMO single crystals on aspects related to electronic mobility, oxygen diffusivity, microstructural evolution regarding to the formation of the highly resistive transition layer using specimens contacted with various electrode metals could help to verify the conception introduced in the present work.

Acknowledgements

The authors gratefully acknowledge essential contributions by Professor Dr. Toru Ishigaki, Frontier Research Center for Applied Atomic Sciences, Ibaraki University (Japan) supporting crystallographic analysis by neutron diffraction experiments. Likewise, Dipl.-Ing. Jochen Friedrich is thankfully acknowledge for tireless technical support.

References

[1] J.M.D. Coey, M. Viret, Mixed-valence manganites, Adv. Phys. 48 (1999) 167-293.
[2] M.B. Salamon, M. Jaime, The physics of manganites: Structure and transport, Rev. Mod. Phys. 73 (2001) 583-628.
[3] Y. Tokura, Correlated-electron physics in transition-metal oxides, Phys. Today 56 (2003) 50-55.
[4] J.M.D. Coey, Charge ordering in oxides, Nature 430 (2004) 155-157.
[5] E. Dagotto, Complexity in strongly correlated electronic systems, Science 309 (2005) 257-262.
[6] T. Venkatesan, M. Rajeswari, Z.-W. Dong, S.B. Ogale, R. Ramesh, Manganite-based devices: opportunities, bottlenecks and challenges, Philos. T. R. Soc. Lond. A 356 (1998) 1661-1680.
[7] G.H. Jonker, J.H. Van Santen, Ferromagnetic compounds of manganese with perovskite structure, Physica 16 (1950) 337-349.
[8] J.H. Van Santen, G.H. Jonker, Electrical conductivity of ferromagnetic compounds of manganese with perovskite structure, Physica 16 (1950) 599-600.
[9] G.H. Jonker, Semiconducting properties of mixed crystals with perovskite structure, Physica 20 (1954) 1118-1122.
[10] G.H. Jonker, Magnetic compounds with perovskite structure – Conducting and non-conducting compounds, Physica 22 (1956) 707-722.
[11] S.B. Adler, Factors governing oxygen reduction in solid oxide fuel cell cathodes, Chem. Rev. 104 (2004) 4791-4843.
[12] J. Parravano, Catalytic activity of lanthanum and strontium manganites, J. Am. Chem. Soc. 75 (1953) 1497-1498.
[13] R.J.H. Voorhoeve, J.P. Remeika, P.E. Freeland, B.T. Matthias, Rare-earth oxides of manganese and cobalt rival platinum for the treatment of carbon monoxide in auto exhaust, Science 177 (1972) 353-354.
[14] R.J.H. Voorhoeve, J.P. Remeika, D.W. Johnson jr., Rare-earth manganites: Catalysts with low ammonia yield in the reduction of nitrogen oxide, Science 180 (1973) 62-64.
[15] E.G. Vrieland, The activity and selectivity of Mn^{3+} and Mn^{4+} in lanthanum calcium manganites for the oxidation of ammonia, J. Catal. 32 (1974) 415-428.
[16] S. Jin, T.H. Tiefel, M. McCormack, R.A. Fastnacht, R. Ramesh, L.H. Chen, Thousandfold change in resistivity in magnetoresistive La-Ca-Mn-O films, Science 264 (1994) 413-415.
[17] L. Ranno, M. Viret, F. Valentin, J. McCauley, J.M.D. Coey, Transport and magnetic properties of $A^{3+}_{1-x}B^{2+}_{x}MnO_3$ (A = La, Y or Nd, B = Ca, Sr or Ba) magnetic perovskites, J. Magn. Magn. Mater. 157/158 (1996) 291-292.
[18] N. Mathur, Not just a load of bolometers, Nature 390 (1997) 229-230.
[19] A.P. Ramirez, Colossal magnetoresistance, J. Phys. Condens. Matter 9 (1997) 8171-8199.
[20] Y. Tokura, Y. Tomioka, Colossal magnetoresistive manganites, J. Magn. Magn. Mater. 200 (1999) 1-23.
[21] E. Dagotto, T. Hotta, A. Moreo, Colossal magnetoresistant materials: The key role of phase separation, Phys. Rep. 344 (2001) 1-153.
[22] C. Israel, M.J. Calderón, N.D. Mathur, The current spin on manganites, Mater. Today 10 (2007) 24-32.
[23] Y. Chen, ReRAM: History, status, and future, IEEE Trans. Electron Devices 67 (2020) 1420-1433.
[24] T.W. Hickmott, Low-frequency negative resistance in thin anodic oxide films. J. Appl. Phys. 33 (1962) 2669-2682.
[25] J.F. Gibbons, W.E. Beadle, Switching properties of thin NiO films, Solid State Electron. 7 (1964) 785-797.
[26] J.C. Bruyere, B.K. Chakraverty, Switching and negative resistance in thin films of nickel oxide, Appl. Phys. Lett. 16 (1970) 40-43.
[27] W.R. Hiatt, T.W. Hickmott, Bistable switching in niobium oxide diodes, Appl. Phys. Lett. 6 (1965) 106-108.
[28] T.W. Hickmott, Electroluminescence, bistable switching, and dielectric breakdown of Nb_2O_5 diodes, J. Vac. Sci. Technol. 6 (1969) 828-833.
[29] F. Argall, Switching phenomena in titanium oxide thin films, Solid State Electron. 11 (1968) 535-541.
[30] H. Pagnia, N. Sotnik, Bistable switching in electroformed metal-insulator-metal devices, Phys. Status Solidi A 108 (1988) 11-65.
[31] A. Asamitsu, Y. Tomioka, H. Kuwahara, Y. Tokura, Current switching of resistive states in magnetoresistive manganites, Nature 388 (1997) 50-52.
[32] H. Oshima, K. Miyano, Y. Konishi, M. Kawasaki, Y. Tokura, Switching behavior of epitaxial perovskite manganite thin films, Appl. Phys. Lett. 75 (1999) 1473-1475.
[33] V. Ponnambalam, S. Parashar, A.R. Raju, C.N.R. Rao, Electric-field-induced insulator-metal transition in thin films of charge-ordered rare-earth manganites, Appl. Phys. Lett. 74 (1999) 206-208.
[34] A. Beck, J.G. Bednorz, Ch. Gerber, C. Rossel, D. Widmer, Reproducible switching effect in thin oxide films for memory applications, Appl. Phys. Lett. 77 (2000) 139-141.
[35] Y. Watanabe, J.G. Bednorz, A. Bietsch, Ch. Gerber, D. Widmer, A. Beck, S.J. Wind, Current-driven insulator-conductor transition and nonvolatile memory in chromium-doped $SrTiO_3$ single crystals, Appl. Phys. Lett. 78 (2001) 3738-3740.
[36] A. Schmehl, F. Lichtenberg, H. Bielefeldt, J. Mannhart, D.G. Schlom, Transport properties of $LaTiO_{3+x}$ films and heterostructures, Appl. Phys. Lett. 82 (2003) 3077-3079.
[37] A. Sawa, T. Fujii, M. Kawasaki, Y. Tokura, Interface resistance switching at a few nanometer thick perovskite manganite active layer, Appl. Phys. Lett. 88 (2006) 232112.
[38] M. Hasan, R. Dong, H.J. Choi, D.S. Lee, D.-J. Seong, M.B. Pyun, H. Hwang, Uniform resistive switching with a thin reactive metal interface layer in metal-$La_{0.7}Ca_{0.3}MnO_3$-metal heterostructures, Appl. Phys. Lett. 92 (2008) 202102.
[39] W. Yu, X. Li, Y. Rui, X. Liu, Q. Wang, L. Chen, Improvement of resistive switching property in a noncrystalline and low-resistance $La_{0.7}Ca_{0.3}MnO_3$ thin film by using an Ag-Al alloy electrode, J. Phys. D: Appl. Phys. 41 (2008) 215409.
[40] R. Yang, X.M. Li, W.D. Yu, X.D. Gao, D.S. Shang, X.J. Liu, X. Cao, Q. Wang, L.D. Chen, The polarity origin of the bipolar resistance switching behaviors in metal/$La_{0.7}Ca_{0.3}MnO_3$/Pt junctions, Appl. Phys. Lett. 95 (2009) 072105.
[41] T. Yamamoto, R. Yasuhara, I. Ohkubo, H. Kumigashira, M. Oshima, Formation of transition layers at metal/perovskite oxide interfaces showing resistive switching behaviors, J. Appl. Phys. 110 (2011) 053707.
[42] K.L. Chopra, Avalanche-induced negative resistance in thin oxide films, J. Appl. Phys. 36 (1965) 184-187.
[43] S.R. Ovshinsky, Reversible electrical switching phenomena in disordered structures, Phys. Rev. Lett. 21 (1968) 1450-1453.
[44] G. Dearnaley, A.M. Stoneham, D.V. Morgan, Electrical phenomena in amorphous oxide films, Rep. Prog. Phys. 33 (1970)1129-1191.
[45] J.S. Lee, S. Lee, T.W. Noh, Resistive switching phenomena: A review of statistical physics approaches, Appl. Phys. Rev. 2 (2015) 031303.
[46] R. Waser, M. Aono, Nanoionics-based resistive switching memories, Nat. Mater. 6 (2007) 833-840.
[47] A. Sawa, Resistive switching in transition metal oxides, Mater. Today 11 (2008) 28-36.
[48] R. Waser, R. Dittmann, G. Staikov, K. Szot, Redox-based resistive switching memories – Nanoionic mechanisms, prospects, and challenges, Adv. Mater. 21 (2009) 2632-2663.
[49] S.Q. Liu, N.J. Wu, A. Ignatiev, Electric-pulse-induced reversible resistance change effect in magnetoresistive films, Appl. Phys. Lett. 76 (2000) 2749-2751.
[50] A. Baikalov, Y.Q. Wang, B. Shen, B. Lorenz, S. Tsui, Y.Y. Sun, Y.Y. Xue, C.W. Chu, Field-driven hysteretic and reversible resistive switch at the Ag-$Pr_{0.7}Ca_{0.3}MnO_3$ interface, Appl. Phys. Lett. 83 (2003) 957-959.
[51] Y. Tomioka, A. Asamitsu, Y. Moritomo, Y. Tokura, Anomalous magnetotransport properties of $Pr_{1-x}Ca_xMnO_3$, J. Phys. Soc. Jpn. 64 (1995) 3626-3630.
[52] Y. Tomioka, A. Asamitsu, H. Kuwahara, Y. Moritomo, Y. Tokura, Magnetic-field-induced metal-insulator phenomena in $Pr_{1-x}Ca_xMnO_3$ with controlled charge-ordering instability, Phys. Rev. B 53 (1996) R1689-R1692.
[53] S. Tsui, A. Baikalov, J. Cmaidalka, Y.Y. Sun, Y.Q. Wang, Y.Y. Xue, C.W. Chu, Field-induced resistive switching in metal-oxide interfaces, Appl. Phys. Lett. 85 (2004) 317-319.
[54] S.Q. Liu, N.J. Wu, A. Ignatiev, J.R. Li, Electric-pulse-induced capacitance change effect in perovskite oxide thin films, J. Appl. Phys. 100 (2006) 056101.
[55] X. Chen, N.J. Wu, J. Strozier, A. Ignatiev, Direct resistance profile for an electrical pulse induced resistance change device, Appl. Phys. Lett. 87 (2005) 233506.
[56] A. Sawa, T. Fujii, M. Kawasaki, Y. Tokura, Interface transport properties and resistance switching in perovskite-oxide heterojunctions, Proc. SPIE 5932 (2005) 59322C.
[57] Y.B. Nian, J. Strozier, N.J. Wu, X. Chen, A. Ignatiev, Evidence for an oxygen diffusion model for the electric pulse induced resistance change effect in transition metal oxides, Phys. Rev. Lett. 98 (2007) 146403.
[58] A. Sawa, T. Fujii, M. Kawasaki, Y. Tokura, Hysteretic current-voltage characteristics and resistance switching at a rectifying Ti/$Pr_{0.7}Ca_{0.3}MnO_3$ interface, Appl. Phys. Lett. 85 (2004) 4073-4075.
[59] Z.L. Liao, Z.Z. Wang, Y. Meng, Z.Y. Liu, P. Gao, J.L. Gang, H.W. Zhao, X.J. Liang, X.D. Bai, D.M. Chen, Categorization of resistive switching of metal-$Pr_{0.7}Ca_{0.3}MnO_3$-metal devices, Appl. Phys. Lett. 94 (2009) 253503.
[61] K. Tsubouchi, I. Ohkubo, H. Kumigashira, M. Oshima, Y. Matsumoto, K. Itaka, T. Ohnishi, M. Lippmaa, H. Koinuma, Adv. Mater. 19 (2007) 1711-1713.
[62] K. Shono, H. Kawano, T. Yokota, M. Gomi, Origin of negative differential resistance observed on bipolar resistance switching device with Ti/$Pr_{0.7}Ca_{0.3}MnO_3$/Pt structure, Appl Phys. Express 1 (2008) 055002.

[63] H. Kawano, K. Shono, T. Yokota, M. Gomi, Enhancement of switching capability on bipolar resistance switching device with Ta/$Pr_{0.7}Ca_{0.3}MnO_3$/Pt structure, Appl. Phys. Express 1 (2008) 101901.

[64] E.I. Goldyreva, I.A. Leonidov, M.V. Patrakeev, V.L. Kozhevnikov, Oxygen non-stoichiometry and defect equilibria in $CaMnO_{3-\delta}$, J. Solid State Electr. 16 (2012) 1187-1191.

[65] N. Kamegashira, Y. Miyazaki, Oxygen pressures over $LaMnO_{3+x}$, Mater. Chem. Phys. 11 (1984) 187-194.

[66] J.H. Kuo, H.U. Anderson, D.M. Sparlin, Oxidation-reduction behaviour of undoped and Sr-doped $LaMnO_3$: Nonstoichiometry and defect structure, J. Solid State Chem. 83 (1989) 52-60.

[67] J.H. Kuo, H.U. Anderson, D.M. Sparlin, Oxidation-reduction behaviour of undoped and Sr-doped $LaMnO_3$: Defect structure, electric conductivity, and thermoelectric Power, J. Solid State Chem. 87 (1990) 55-63.

[68] J.A.M. Van Roosmalen, E.H.P. Cordfunke, A new defect model to describe the oxygen deficiency in perovskite-type oxides, J. Solid State Chem. 93 (1991) 212-219.

[69] J.A.M. Van Roosmalen, E.H.P. Cordfunke, R.B. Helmholdt, H.W. Zandbergen, The defect chemistry of $LaMnO_{3\pm\delta}$ – 2. Structural aspects of $LaMnO_{3+\delta}$, J. Solid State Chem. 110 (1994) 100-105.

[70] J.A.M. Van Roosmalen, E.H.P. Cordfunke, The defect chemistry of $LaMnO_{3\pm\delta}$ – 3. The density of (La, A)$MnO_{3+\delta}$ (A = Ca, Sr, Ba), J. Solid State Chem. 110 (1994) 106-108.

[71] J.A.M. Van Roosmalen, E.H.P. Cordfunke, The defect chemistry of $LaMnO_{3\pm\delta}$ – 4. Defect model for $LaMnO_{3+\delta}$, J. Solid State Chem. 110 (1994) 109-112.

[72] J.A.M. Van Roosmalen, E.H.P. Cordfunke, The defect chemistry of $LaMnO_{3\pm\delta}$ – 5. Thermodynamics, J. Solid State Chem. 110 (1994) 113-117.

[73] H. Kamata, Y. Yonemura, J. Mizusaki, H. Tagawa, K. Naraya, T. Sasamoto, High temperature electrical properties of the perovskite-type oxide $La_{1-x}Sr_xMnO_{3-\delta}$, J. Phys. Chem. Solids 56 (1995) 943-950.

[74] J. Nowotny, M. Rekas, Defect chemistry of (La, Sr)MnO_3, J. Am. Ceram. Soc. 81 (1998) 67-80

[75] F.W. Poulsen, Defect chemistry modelling of oxygen-stoichiometry, vacancy concentration, and conductivity of $(La_{1-x}Sr_x)_yMnO_{3\pm\delta}$, Solid State Ionics 129 (2000) 145-162.

[76] J. Mizusaki, N. Mori, H. Takai, Y. Yonemura, H. Minamiue, H. Tagawa, M. Dokiya, H. Inaba, K. Naraya, T. Sasamoto, T. Hashimoto, Oxygen nonstoichiometry and defect equilibrium in the perovskite-type oxide $La_{1-x}Sr_xMnO_{3+d}$, Solid State Ionics 129 (2000) 163-177.

[77] J. Mizusaki, Y. Yonemura, H. Kamata, K. Ohyama, N. Mori, H. Takai, H. Tagawa, M. Dokiya, K. Naraya, T. Sasamoto, H. Inaba, T. Hashimoto, Electronic conductivity, Seebeck-coefficient, defect and electronic structure of nonstoichiometric $La_{1-x}Sr_xMnO_3$, Solid State Ionics 129 (2000) 167-180.

[78] R. Meyer, L. Schloss, J. Brewer, R. Lambertson, W. Kinney, J. Sanchez, D. Rinerson, Oxide dual-layer memory element for scalable non-volatile cross-point memory technology, Proc. of the Non-Volatile Memory Technology Symposium (2008) 54-59.

[79] F. Borgatti, C. Park, A. Herpers, F. Offi, R. Egoavil, Y. Yamashita, A. Yang, M. Kobata, K. Kobayashi, J. Verbeeck, G. Panaccione, R. Dittmann, Chemical insight into electroforming of resistive switching manganite heterostructures, Nanoscale 5 (2013) 3954-3960.

[80] A. Herpers, C. Lenser, C. Park, F. Offi, F. Borgatti, G. Panaccione, S. Menzel, R. Waser, R. Dittmann, Spectroscopic proof of the correlation between redox-state and charge-carrier transport at the interface of resistively switching Ti/PCMO devices, Adv. Mater. 26 (2014) 2730-2735.

[81] B. Arndt, F. Borgatti, F. Offi, M. Phillips, P. Parreira, T. Meiners, S. Menzel, K. Skaja, G. Panaccione, D.A. MacLaren, R. Waser, R. Dittmann, Spectroscopic indications of tunnel barrier charging as the switching mechanism in memristive devices, Adv. Funct. Mater. 27 (2017) 1702282.

[82] J. Norpoth, S. Mildner, M. Scherff, J. Hoffmann, C. Jooss, In situ TEM analysis of resistive switching in manganite based thin-film heterostructures, Nanoscale 6 (2014) 9852-9862.

[83] Y. Wang, K.-M. Kang, M. Kim, H.-S. Lee, R. Waser, D. Wouters, R. Dittmann, J.J. Yang, H.-H. Park, Mott-transition-based RRAM, Mat. Today 28 (2019) 63-80.

[84] M. Scherff, J. Hoffmann, B. Meyer, Th. Danz, Ch. Jooss, Interplay of cross plane polaronic transport and resistive switching in Pt-$Pr_{0.67}Ca_{0.33}MnO_3$-Pt, New J. Phys. 15 (2013) 103008.

[85] M.J. Rozenberg, I.H. Inoue, M.J. Sánchez, Strong electron correlation effects in non-volatile electronic memory devices, Appl. Phys. Lett. 88 (2006) 033510.

[86] M. Quintero, P. Levy, A.G. Leyva, M.J. Rozenberg, Mechanism of electric-pulse-induced resistance switching in manganites, Phys. Rev. Lett. 98 (2007) 116601.

[87] K.R. Poeppelmeier, M.E. Leonowicz, J.C. Scanlon, J.M. Longo, W.B. Yelon, Structure determination of $CaMnO_3$ and $CaMnO_{2.5}$ by X-ray and neutron methods, J. Solid State Chem. 45 (1982) 71-79.

[88] B. Dabrowski, S. Kolesnik, A. Baszczuk, O. Chmaissem, T. Maxwell, J. Mais, Structural, transport, and magnetic properties of $RMnO_3$ perovskites (R = La, Pr, Nd, Sm ^{153}Eu, Dy), J. Solid State Chem. 178 (2005) 629-637.

[89] L.M.G. Dortmans, R. Morrell, G. de With, Round robin on grain size measurement for advanced technical ceramics, J. Eur. Ceram. Soc. 12 (1993) 205-213.

[90] G.S. Pawley, Unit-cell refinement from powder diffraction scans, J. Appl. Cryst. 14 (1981) 357-361.

[91] F. Licci, G. Turilli, P. Ferro, Determination of manganese valence in complex La-Mn perovskites, J. Magn. Magn. Mater. 164 (1996) L268-L272.

[92] H.Taguchi, Electrical properties of $CaMnO_{3-\delta}$, Phys. Status Solidi A (1985) K79-K82.

[93] M. Ohtaki, H. Koga, T. Tokunaga, K. Eguchi, H. Arai, Electrical transport properties and high-temperature thermoelectric performance of $(Ca_{0.9}M_{0.1})MnO_3$ (M = Y, La, Ce, Sm, In, Sn, Sb, Pb, Bi), J. Solid State Chem. 120 (1995) 105-111.

[94] H. Taguchi, M. Sonoda, M. Nagao, Relationship between angles for Mn-O-Mn and electrical properties of orthorhombic perovskite-type $(Ca_{1-x}Sr_x)MnO_3$, J. Solid State Chem. 137 (1998) 82-86.

[95] M.E. Melo Jorge, A. Correia dos Santos, M.R. Nunes, Effects of synthesis method on stoichiometry, structure and electrical conductivity of $CaMnO_{3-\delta}$, Int. J. Inorg. Mater. 3 (2001) 915-921.

[96] B.T. Cong, T. Tsuji, P.X. Thao, P.Q. Thanh, Y. Yamamura, High-temperature thermoelectric properties of $Ca_{1-x}Pr_xMnO_{3-\delta}$ ($0 \le x < 1$), Physica B 352 (2004) 18-23.

[97] H. Taguchi, M. Nagao, T. Sato, M. Shimada, High-temperature phase transition of $CaMnO_{3-\delta}$, J. Solid State Chem. 78 (1989) 312-315.

[98] E.I Leonidova, I.A. Leonidov, M.V. Patrakeev, V.L. Kozhevnikov, Oxygen non-stoichiometry, high-temperature properties, and phase diagram of $CaMnO_{3-\delta}$, J. Solid State Electr. 15 (2011) 1071-1075.

[99] Y. Wang, Y. Sui, J. Cheng, X. Wang, Z. Lu, W. Su, High-temperature metal-insulator transition induced by rare-earth doping in perovskite $CaMnO_3$, J. Phys. Chem. C 113 (2009) 12509-12516.

[100] R.-Z. Yin, C.H. Yo, Unusual magnetic and transport properties of the CMR $Pr_{1-x}Ca_xMnO_{3-y}$ system, J. Mater. Sci. 42 (2007) 660-668.

[101] A.T. Kozakov, A.G. Kochur, V.G. Trotsenko, A.V. Nikolskii, M. El Marssi, B.P. Gorshunov, V.I. Torgashev, Valence state of cations in manganites $Pr_{1-x}Ca_xMnO_3$ ($0.3 \le x \le 0.5$) from X-ray diffraction and X-ray photoelectron spectroscopy, J. Alloys Compd. 740 (2018) 132-142.

[102] J.A. Collado, C. Frontera, J.L. García-Munos, C. Ritter, M. Brunelli, M.A.G. Aranda, Room temperature structural and microstructural study for the magneto-conducting $La_{5/8-x}Pr_xCa_{3/8}MnO_3$ ($0 \le x \le 5/8$) series, Chem. Mater. 15 (2003) 167-174.

[103] D.C. Krishna, P. Venugopal Reddy, Magnetic transport behavior of nano-crystalline $Pr_{0.67}A_{0.33}MnO_3$ (A = Ca, Sr, Pb and Ba) manganites, J. Alloys Compd. 479 (2009) 661-669.

[104] N. Guiblin, D. Grebille, C. Martin, M. Hervieu, Praseodymium magnetic contribution in the low temperature structure of $Pr_{0.8}Ca_{0.2}MnO_3$, J. Solid State Chem. 177 (2004) 3310-3315.

[105] Z. Jirák, S. Vratislav, J. Zajíček, The magnetic structure of $Pr_{0.9}Ca_{0.1}MnO_3$, Phys. Status Solidi A 52 (1979) K39-K43.

[106] R.D. Shannon, C.T. Prewitt, Effective ionic radii in oxides and fluorides, Acta Crystallogr. B25 (1969) 925-946.

[107] R.D. Shannon, Revised effective ionic radii and systematic studies of interatomic distances in halides and chalcogenides, Acta Crystallogr. A32 (1976) 751-767.

[108] V.M. Goldschmidt, Die Gesetze der Krystallochemie, Naturwissenschaften 21 (1926) 477-485.

[109] S. Schramm, J. Hoffmann, Ch. Jooss, Transport and ordering of polarons in CER manganites PrCaMnO, J. Phys. Condens. Matter 20 (2008) 395231.

[110] E.I. Goldyreva, I.A. Leonidov, M.V. Patrakeev, V.L. Kozhevnikov, Temperature activated electron transport in CaMnO3, Solid State Ionics 262 (2014) 678-681.

[111] R.R. Heikes, Thermoelectricity, Interscience, New York, 1961.

[112] Z. Liao, P. Gao, X. Bai, D. Chen, J. Zhang, Evidence for electric-field-driven migration and diffusion of oxygen vacancies in $Pr_{0.7}Ca_{0.3}MnO_3$, J. Appl. Phys. 111 (2012) 114506.